


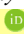
Isotope Chronology and Geochemistry of the Lower Carboniferous Granite in Xilinhot, Inner Mongolia, China

Xiaocheng Zhao¹, Wenxiao Zhou^{2*}, Dong Fu³, Bo Huang³, Mengchun Ge³

1. Geotechnical & Structural Engineering Research Center, Shandong University, Jinan 250061, China

2. Institute of Geological Survey, China University of Geosciences, Wuhan 430074, China

3. School of Earth Sciences, China University of Geosciences, Wuhan 430074, China

 Xiaocheng Zhao: <https://orcid.org/0000-0003-4474-9817>;  Wenxiao Zhou: <https://orcid.org/0000-0003-4890-8803>

ABSTRACT: Geochronological and geochemical analyses were performed on K-feldspar granites and monzonitic granites from the Xilinhot area, Inner Mongolia, China. Zircon U/Pb ages indicate that the two types granites were emplaced during the Lower Carboniferous. The K-feldspar granites (332 Ma) have the typical A-type granite characteristics of a post-collision setting. The monzonitic granites have an emplacement age of 323 Ma. Zircon ϵ_{Hf} values of the former range from +12.8 to +14.2, with an average T_{DM2} of 453 Ma. The latter have lower zircon ϵ_{Hf} values, ranging from +5.4 to +10.7, with an average T_{DM2} of 798 Ma. The strong, positive ϵ_{Hf} values of the zircon indicate that both sets of samples are from a juvenile crust formed in an oceanic crust subduction stage, although the monzonitic granite may have undergone a hybridization of crustal materials. These results indicate a younger post orogenic event. The Paleo-Asian Ocean had closed before the Early Carboniferous and the Xilinhot area started its post-orogenic evolution with an extensional tectonic environment during the Early Carboniferous.

KEY WORDS: Lower Carboniferous granite, Paleo-Asian Ocean, Lu-Hf isotope, Xilinhot, Inner Mongolia.

0 INTRODUCTION

The Central Asian orogenic belt (CAOB) is an ancient accretion-type orogenic belt located between the Siberian Plate and the North China Plate (Jian et al., 2008), and it presents a series of island arcs as well as forearc and back-arc basins, an ophiolitic belt, and microcontinents formed from the Neoproterozoic to the Mesozoic (Xu et al., 2013; Glorie et al., 2011; Kröner et al., 2011, 2010, 2007; Demoux et al., 2009; Xiao et al., 2009, 2003; Li, 2006; Buslov et al., 2004; Khain et al., 2003, 2002; Badarch et al., 2002; Şengör and Natal'in, 1996; Mossakovsky et al., 1994; Şengör et al., 1993; Hsu et al., 1991). In addition, the massive juvenile crust materials were formed during this period (Ma et al., 2017; Xu et al., 2013; Wang et al., 2012; Han et al., 2011, 1997; Jahn et al., 2009, 2000a, b; Hong et al., 2004, 1995). However, the tectonic evolution of this region during the Late Paleozoic and the closing time of the Paleo-Asian Ocean remain unclear.

One hypothesis asserts that the Paleo-Asian Ocean closed because of a collision between the Siberian and the North China plates, which occurred before the Late Devonian (Shao et al., 2014; Xu et al., 2014; Xu and Chen, 1997; Hong et al., 1994; Tang, 1992, 1990). However, another hypothesis states that the collisional orogenesis continued until the Late Permian–Early Triassic (Zhang and Zhai, 2010; Li et al., 2007; Zhang et al.,

2006) and occurred concurrently with an Andean-type continental margin.

In this paper, the latest data on two genetic types of granite found in the Xilinhot area were obtained based on regional geological surveys as well as petrographic, geochemical and zircon U-Pb and Lu-Hf isotope analyses of the granites, and we provide new evidence on the tectonic evolution of the CAOB.

1 GEOLOGIC SETTING AND PETROGRAPHY

Based on the demarcation of geotectonic units, the Xilinhot area belongs to the suture zone that developed after the subduction and collision between the Siberian Plate and the North China Plate. The suture zone extends from the Solonker Mountains along the Sonidzuoqi and continues eastward to the Xilinhot area, and this zone represents the location of the Paleo-Asian Ocean subduction (Xu and Chen, 1997). After performing detailed surveys and field research, we discovered multistage intrusive rocks from the Carboniferous Period to the south and southeast of Xilinhot City, including A-type K-feldspar granite, monzonitic granite, granodiorite, and gabbro.

The Early Carboniferous A-type K-feldspar granites, which were mainly distributed on the northwest side of the Daituojika Mountain (Fig. 1), intruded into the schists of the Ordovician Bulongshan Group and were covered by glutenites of the Lower Jurassic Hongqi Group. These Early Paleozoic glutenites were then intruded by granodiorites (Zhou et al., 2016) of the Late Carboniferous and diorites of the Early Permian Period. The monzonitic granites of the Early Carboniferous Period were output as stocks, bosses, and dykes, and they intruded the biotite-plagioclase gneiss of the Early–Late

*Corresponding author: zhouwenxiao@cug.edu.cn

© China University of Geosciences and Springer-Verlag GmbH Germany, Part of Springer Nature 2018

Manuscript received January 25, 2016.

Manuscript accepted September 15, 2016.

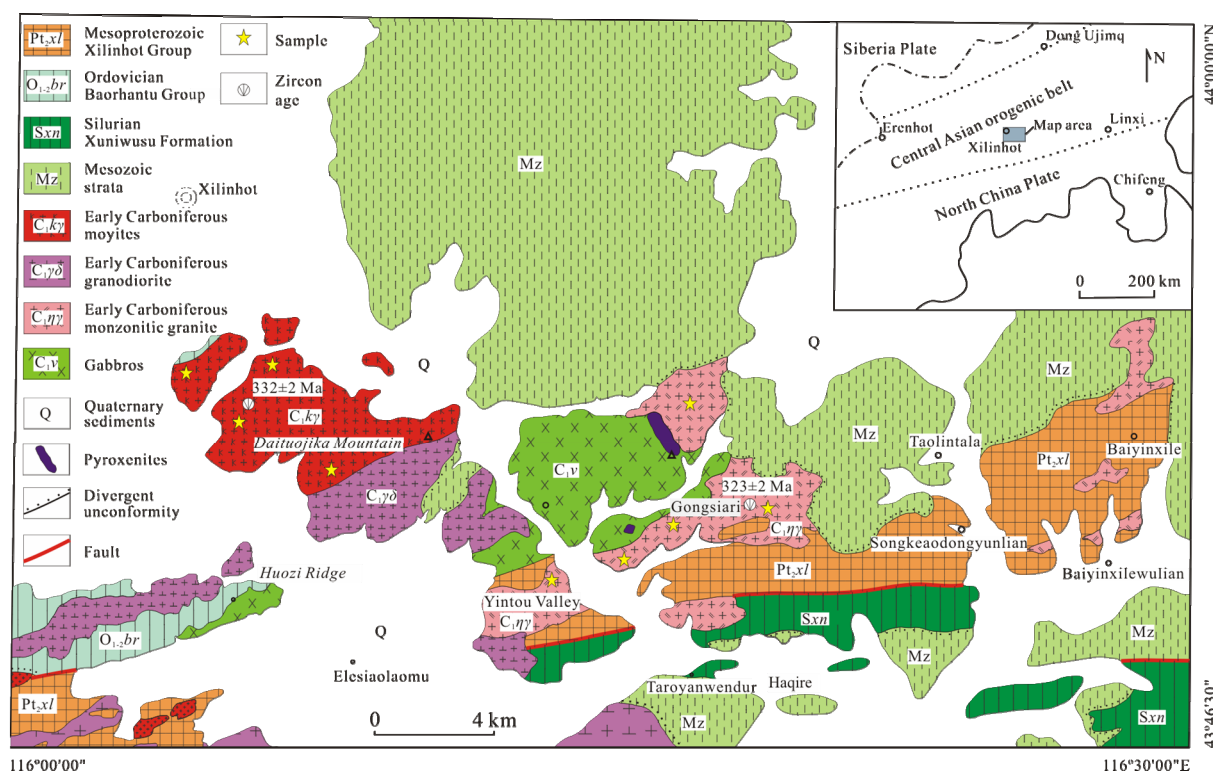


Figure 1. Regional geological map of the Xilinhot area in Inner Mongolia (modified after Zhou et al., 2016).

Proterozoic. Subsequently, these granites were overlain by an unconformity of volcanic rocks of the Meiletu Group of the Lower Jurassic Period and then intruded by the gabbro and granodiorite (Zhou et al., 2016) of the Late Carboniferous Period. In the Yintou Valley, Saqinhua, Shihuiyao, and Gongsiazi areas, prominent outcrops can be observed.

The A-type K-feldspar granites have a fresh pink color, exhibit subhedral-anhedral granules, and are fine-to-medium grained (Figs. 2a, 2b). These granites consist of K-feldspar (63%–66%; anhedral granules; 0.3–0.5 mm in diameter; and internal microcrystals of plagioclase), quartz (19%–22%; anhedral granules; 0.5–1 mm in diameter; and internal microcrystals of plagioclase and K-feldspar that constitute a graphic texture with K-feldspar), and plagioclase (15%; subhedral tabular granules; 0.3–1.5 mm; albite twins; and $Np^{(10)}=13^\circ$, which represents oligoclase).

The monzonitic granites are off-white in color at the fresh surfaces, and under a polarizing microscope, the minerals are subhedral and fine-to-medium grained (Figs. 2c, 2d). The monzonite granites consist of plagioclase (45%; subhedral tabular granules; 0.5–1.5 mm; albite twins; $Np^{(10)}=12^\circ\text{--}15^\circ$, which represents oligoclase or andesine; and sericitization), K-feldspar (25%; anhedral granules; and 0.5–1.5 mm in diameter), quartz (25%; anhedral granules; and 0.5–1.5 mm in diameter), biotite (3%; flaky; ~ 0.8 mm; and little chloritization), and muscovite (2%; thin film; and 0.5–1 mm).

2 ANALYTICAL METHODS

2.1 Zircon Morphology

The sample processing for the zircon separation involved crushing, initial heavy liquid separation, and subsequent magnetic separation. The representative zircons were manually selected and mounted on adhesive tape, embedded in epoxy resin, polished to

approximately half their size, and then photographed in reflected and transmitted light (Song et al., 2002). The zircon structure and origin were studied by cathodoluminescence (CL) imaging of the zircon grains using a Quanta 400FEG environmental scanning electron microscope equipped with an Oxford spectrometer and a Gatan CL3+ detector at the State Key Laboratory of Continental Dynamics, Northwest University, Xi'an, China. The accelerating voltage was 10 kV, and the beam current was 240 μA .

Zircon LA-ICP-MS U-Pb dating was conducted at the Isotope Laboratory of Tianjin Center, China Geological Survey, using a neptune MC-ICP-MS with a UP193-FX ArF-excimer laser-ablation system. The data were collected with a 35 μm spot, and the ablation depth was 20–40 μm . Helium was used as a carrier gas to enhance the transport efficiency of the ablated material. Zircon 91500 was the external standard for the age calculation (Wiedenbeck et al., 1995), NIST SRM 610 silica glass was the external standard for the concentration calculation (Pearce et al., 1997), and Si was the internal standard. The collection mode of the sample was an individual spot ablation, and the data were collected using one massive peak to one spot (peak jumping). We measured NIST SRM610 twice after each round of 15–20 zircon sample spots. The off-line selection and integration of the background and analysis signals and the time-drift correction and quantitative calibration for the trace element analyses and U-Pb dating were performed using ICPMSDataCal (Liu et al., 2009, 2008), and common Pb was corrected according to Andersen (2002). The reported ages were calculated, and concordia diagrams were constructed and weighted mean calculations were performed using the software Isoplot/Ex_Ver3 (Ludwig, 2003).

2.2 Major and Trace Element Analyses

The whole-rock samples were crushed in a corundum jaw

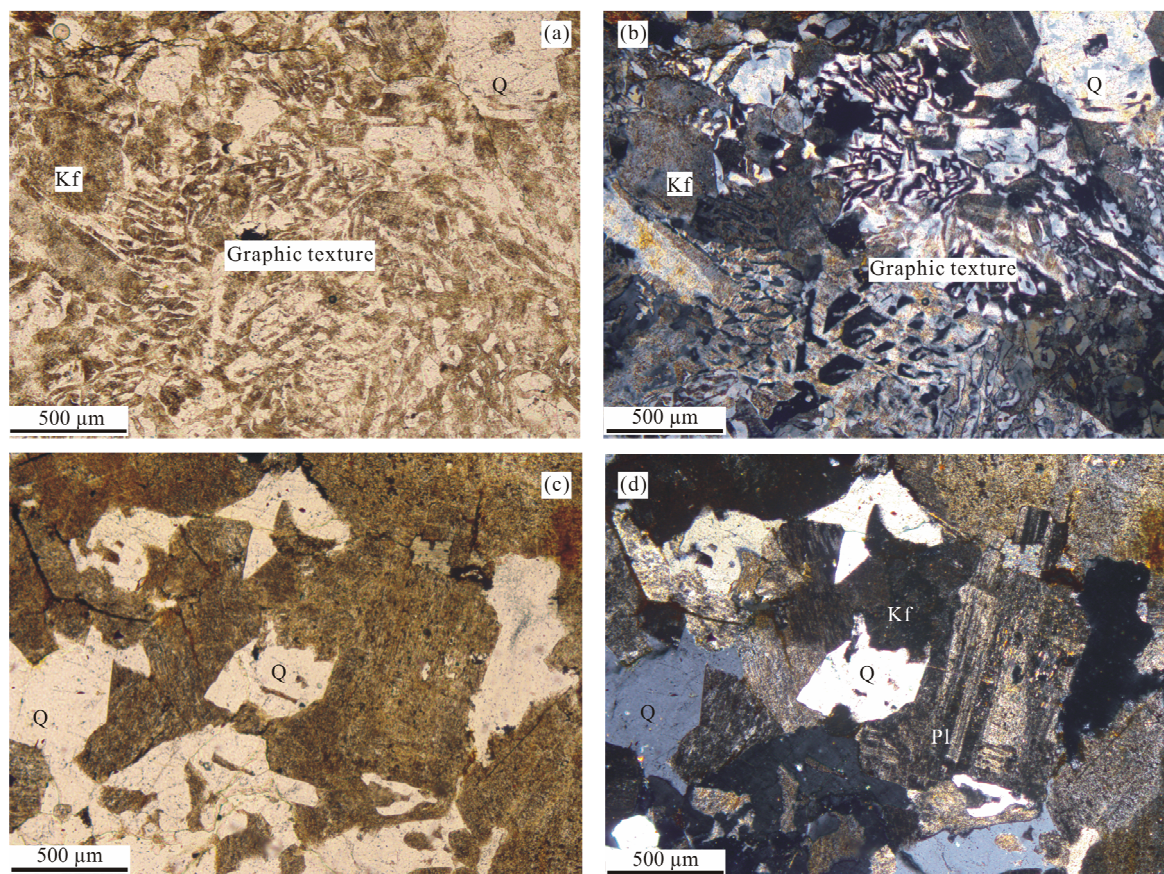


Figure 2. (a), (b) Photomicrographs of the A-type K-feldspar (polar image and crossed polar image); (c), (d) photomicrographs of the monzonitic granite (polar image and crossed polar image). Q. Quartz; Kf. K-feldspar; Pl. plagioclase.

crusher (to a size of 60 mesh). Approximately 60 g was powdered in an agate ring mill to a size of less than 200 mesh. The major element contents of the samples were determined via the X-ray fluorescence analysis of fused glass beads using a spectrometer (3080E1; Rigaku, Tokyo, Japan), and the trace elements were determined by the ICP-MS (X. Series, Thermo Fisher Scientific, Germany) at the Wuhan Rock and Mineral Analysis Center, Ministry of Land and Resources Research, China. The analytical precision and accuracy of these methods were better than 5% for most elements. The ferric-ferrous iron proportions were determined by wet chemistry.

2.3 Zircon Hf Isotopic Analysis

The experiments were conducted using a Neptune Plus MC-ICP-MS (Thermo Fisher Scientific, Germany) in combination with a Geolas 2005 ArF-excimer laser ablation system (Lambda Physik, Göttingen, Germany) that was hosted by the State Key Laboratory of Geological Processes and Mineral Resources, China University of Geosciences in Wuhan. The energy density of the laser ablation used in this study was 5.3 J/cm². A wire signal smoothing device is included in this laser ablation system to ensure the production of smooth signals even at low laser repetition rates of 1 Hz (Hu et al., 2012). Helium was used as the carrier gas within the ablation cell, and it was merged with argon (makeup gas) after the ablation cell. As we previously demonstrated (Hu et al., 2008a), a consistent 2-fold signal enhancement for the 193 nm laser was achieved in

helium, which was more effective than argon gas. We used a simple Y-junction downstream from the sample cell to add small amounts of nitrogen (4 mL·min⁻¹) to the argon makeup gas flow (Hu et al., 2008b). Compared with the standard arrangement, the addition of nitrogen in combination with the use of the newly designed X skimmer cone and the Jet sample cone in the Neptune Plus improved the signal intensity of Hf, Yb and Lu by a factor of 5.3, 4.0 and 2.4, respectively. All of the zircon data were acquired in single spot ablation mode at a spot size of 44 μm. Each measurement consisted of 20 s of acquisition of the background signal followed by 50 s of the ablation signal acquisition. The detailed operating conditions for the laser ablation system and the MC-ICP-MS instrument along with the analytical methods are described in Hu et al. (2012).

3 RESULTS

3.1 Zircon U-Pb Data

The zircon U-Pb analysis results for the two genetic types of granites are listed in Table 1. The zircon samples of the K-feldspar granite acquired from the Daituojika Mountain are mostly euhedral and shortly prismatic, 150–300 μm long, present length/width ratios of 1.5–2.7, and show common and clearly internal oscillatory zoning in the CL images (Fig. 3). Twenty spots of 18 zircons yielded Th/U ratios of 0.56–1.40, which is a distinct feature of magmatic zircons (Wu and Zheng, 2004; Möller et al., 2003; Rubatto and Gebauer, 2000). Except for one analysis, which determined a relatively old age for the

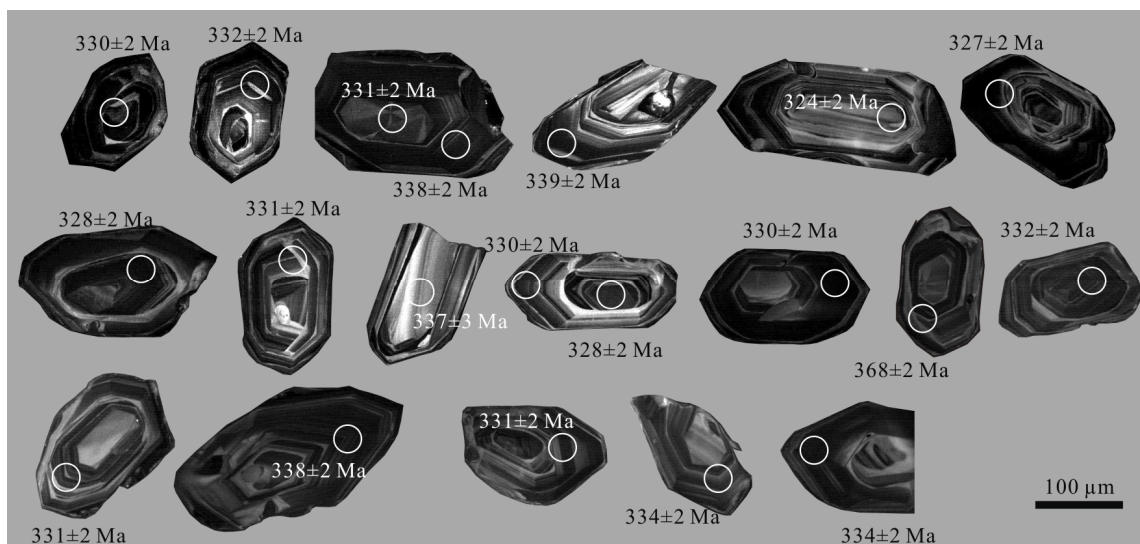


Figure 3. Cathodoluminescence (CL) images of the dated zircons for the K-feldspar granite.

sample (368±2 Ma), the other 19 spots showed consistent age results of 324–339 Ma (Fig. 4a) and a weighted mean $^{206}\text{Pb}/^{238}\text{U}$ age of 332±2 Ma, with a MSWD of 0.19 (Fig. 4b). For the monzonitic granite sample from the Nagawula area in Xilinhot, all of the zircons present a euhedral prismatic structure, are approximately 130–190 µm long, and have length/width ratios ranging from 2 to 3 (Fig. 5). All of the spots have high Th/U ratios of 0.78–1.71, which suggests that these zircons formed from magma. Apart from the 5 sample spots that were not consistent or yielded relatively old ages of 348–387 Ma, the estimated ages of 15 of the 20 tested zircon grains were consistent (Fig. 6a) with the $^{206}\text{Pb}/^{238}\text{U}$ ages ranging of 323–329 Ma. The weighted mean $^{206}\text{Pb}/^{238}\text{U}$ age is 323±2 Ma, with a MSWD of 1.9 (Fig. 6b).

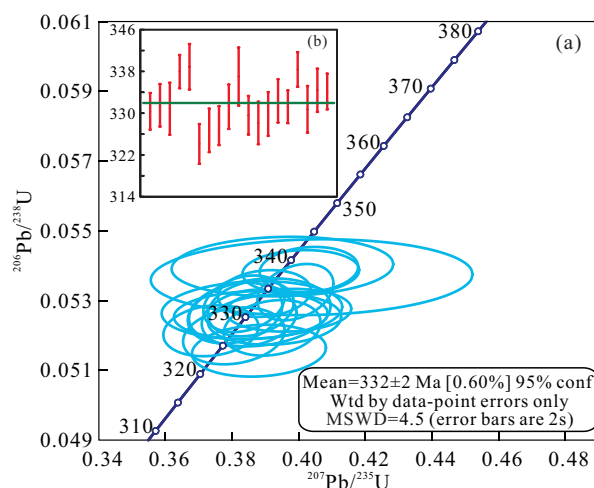


Figure 4. U-Pb zircon concordant age diagram (a) and weighted average age features (b) for the K-feldspar granite from the Xilinhot area.

3.2 Major, Trace, and Rare Earth Elements

Table 2 presents the results for the major, trace, and rare earth element analyses for the two genetic types of granites from



Figure 5. Cathodoluminescence images of the dated zircons for the monzonitic granite.

Table 1 LA-ICP-MS zircon U-Pb data for the two types granites in Xilinhot area

The K-feldspar granites													
Spots	Content		Th/U	Isotopic ratios				Age (Ma)					
	Pb (ppm)	U (ppm)		$^{206}\text{Pb}/^{238}\text{U}$	$^{207}\text{Pb}/^{235}\text{U}$	$^{207}\text{Pb}/^{206}\text{Pb}$	$^{206}\text{Pb}/^{238}\text{U}$	$^{207}\text{Pb}/^{235}\text{U}$	1σ				
1	24	408	0.930 2	0.052 6	0.000 3	0.385 6	0.009 4	0.053 2	0.001 3	330	2	331	8
2	39	655	0.936 1	0.052 8	0.000 3	0.385 6	0.005 3	0.053 0	0.000 7	332	2	331	5
3	26	412	1.122 9	0.052 7	0.000 4	0.388 3	0.008 7	0.053 5	0.001 2	331	2	333	7
4	34	573	0.805 9	0.053 8	0.000 3	0.400 7	0.007 2	0.054 0	0.000 9	338	2	342	6
5	20	337	0.905 9	0.054 0	0.000 3	0.395 1	0.013 6	0.053 1	0.001 8	339	2	338	12
6	26	433	1.037 1	0.051 6	0.000 3	0.388 1	0.008 2	0.054 6	0.001 1	324	2	333	7
7	32	560	0.844 4	0.052 0	0.000 3	0.380 6	0.006 2	0.053 1	0.000 8	327	2	327	5
8	34	590	0.774 1	0.052 1	0.000 3	0.373 6	0.005 8	0.052 0	0.000 8	328	2	322	5
9	23	379	0.816 2	0.052 7	0.000 3	0.386 0	0.011 1	0.053 1	0.001 5	331	2	331	10
10	8	143	0.560 2	0.053 7	0.000 4	0.403 9	0.019 7	0.054 6	0.002 7	337	3	344	17
11	23	404	0.766 9	0.052 5	0.000 3	0.392 8	0.008 2	0.054 3	0.001 1	330	2	336	7
12	36	588	0.985 4	0.052 2	0.000 3	0.392 0	0.005 9	0.054 4	0.000 8	328	2	336	5
13	36	629	0.725 2	0.052 5	0.000 3	0.385 1	0.005 8	0.053 2	0.000 8	330	2	331	5
14	31	443	1.178 4	0.058 8	0.000 3	0.449 7	0.007 7	0.055 5	0.000 9	368	2	377	6
15	45	769	0.881 4	0.052 9	0.000 3	0.383 6	0.005 0	0.052 6	0.000 7	332	2	330	4
16	26	440	1.05	0.052 7	0.000 3	0.397 0	0.007 7	0.054 6	0.001 0	331	2	339	7
17	40	639	1.218 1	0.053 9	0.000 3	0.403 1	0.006 0	0.054 2	0.000 8	338	2	344	5
18	40	660	1.079 2	0.052 6	0.000 4	0.380 9	0.005 8	0.052 5	0.000 8	331	2	328	5
19	56	867	1.401 8	0.053 2	0.000 3	0.399 0	0.004 7	0.054 4	0.000 6	334	2	341	4
20	35	605	0.831 2	0.053 2	0.000 3	0.389 7	0.005 7	0.053 1	0.000 8	334	2	334	5

The monzonitic granites													
Spots	Content		Th/U	Isotopic ratios				Age (Ma)					
	Pb (ppm)	U (ppm)		$^{206}\text{Pb}/^{238}\text{U}$	$^{207}\text{Pb}/^{235}\text{U}$	$^{207}\text{Pb}/^{206}\text{Pb}$	$^{206}\text{Pb}/^{238}\text{U}$	$^{207}\text{Pb}/^{235}\text{U}$	1σ				
1	46	792	0.787 0	0.051 4	0.000 4	0.383 1	0.011 2	0.054 0	0.001 5	323	2	329	10
2	17	240	0.923 2	0.056 4	0.000 7	0.540 5	0.026 2	0.069 6	0.003 4	353	4	439	21
3	24	353	1.514 4	0.052 0	0.000 5	0.390 7	0.019 9	0.054 4	0.002 7	327	3	335	17
4	51	866	0.866 7	0.051 4	0.000 4	0.377 2	0.011 0	0.053 3	0.001 5	323	3	325	9
5	18	304	0.662 3	0.051 7	0.000 4	0.400 8	0.023 0	0.056 2	0.003 1	325	3	342	20
6	34	615	0.543 5	0.052 1	0.000 4	0.390 9	0.012 9	0.054 5	0.001 8	327	2	335	11
7	45	706	0.954 2	0.055 0	0.000 4	0.405 7	0.011 8	0.053 5	0.001 5	345	2	346	10
8	13	149	0.849 9	0.061 9	0.000 8	1.426 0	0.061 7	0.166 8	0.007 0	387	5	900	39
9	36	510	0.864 2	0.055 9	0.000 5	0.648 5	0.019 2	0.084 1	0.002 3	351	3	508	15

Table 1 Continued

Spots		The monzonitic granites												
Pb (ppm)	U (ppm)	Th/U	$^{206}\text{Pb}/^{238}\text{U}$			$^{207}\text{Pb}/^{235}\text{U}$			$^{206}\text{Pb}/^{238}\text{U}$			Age (Ma)		
			1σ	1σ	1σ	1σ	1σ	1σ	1σ	1σ	1σ	1σ	1σ	1σ
28	484	0.9157	0.0511	0.0003	0.3628	0.0132	0.0515	0.0018	321	2	314	11		
33	612	0.5669	0.0514	0.0004	0.3715	0.0132	0.0524	0.0018	323	2	321	11		
25	435	0.7172	0.0521	0.0006	0.3868	0.0164	0.0539	0.0023	327	4	332	14		
8	132	1.0689	0.0506	0.0007	0.3543	0.0423	0.0509	0.0061	318	5	308	37		
38	650	0.8519	0.0509	0.0004	0.3615	0.0107	0.0515	0.0015	320	2	313	9		
50	879	0.6344	0.0524	0.0003	0.3934	0.0099	0.0544	0.0013	329	2	337	8		
39	717	0.5243	0.0513	0.0003	0.3875	0.0106	0.0548	0.0015	322	2	333	9		
40	608	1.7193	0.0504	0.0004	0.3948	0.0136	0.0568	0.0020	317	3	338	12		
46	774	0.8167	0.0513	0.0003	0.3821	0.0110	0.0540	0.0015	323	2	329	9		
24	467	0.3897	0.0509	0.0004	0.3714	0.0152	0.0528	0.0021	320	2	321	13		
13	188	1.1776	0.0550	0.0006	0.4045	0.0339	0.0536	0.0045	345	4	345	29		

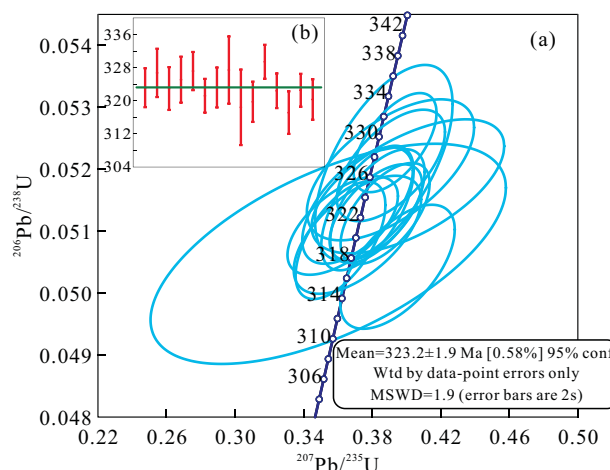


Figure 6. U-Pb Zircon concordant age diagram (a) and weighted average age features (b) for the monzonitic granite from the Xilinhot area.

the Xilinhot area. The K-feldspar granites are highly enriched in SiO₂ (72.94 wt.%–76.66 wt.%), highly alkaline (7.86–8.97), low in Fe and Mg (Fe₂O₃=0.16 wt.%–0.84 wt.%, FeO=0.20 wt.%–0.97 wt.%, MgO=0.09 wt.%–0.29 wt.%), and low in CaO (0.23 wt.%–0.98 wt.%). The average K₂O/Na₂O ratio is 0.93, but the average FeO^T/MgO ratio is higher at 13.6. The samples are mainly ferroan (Fig. 6c) and fall within the alkali field on the alkali-lime index plot (Fig. 6d). In the TAS diagram of intrusive rocks, all 8 samples fall in the sub-alkaline granite field (Fig. 7). Then content of Al₂O₃ presents a restricted range (12.70 wt.%–13.97 wt.%), with A/NK=1.03–1.19 and A/CNK=1.03–1.14. These values suggest that the K-feldspar is peraluminous (Fig. 8). Similar to the results for the trace elements, the K-feldspar granites present high values of total rare earth elements (REEs), are strongly enriched in light rare earth elements (LREEs), have La_N/Yb_N ratios ranging from 3.08 to 9.53, and present obvious negative Eu anomalies (δEu: 0.29–0.53), which is typical of A-type granites. The LREEs show an obvious rightward incline, whereas the HREEs appear as a decline in the rock/chondritic diagram (Fig. 9). In the rock/primitive mantle diagram (Fig. 10), the rocks indicate enrichment in both large ion lithophile elements (LILE), such as Rb, K, and Ba, and in the high field strength elements, such as Th, Nd, Zr, and Hf. However, the Nb, Ta, P, Ti, and Sr elements show obviously negative anomalies.

The analyses for the major, trace, and rare earth elements of the 8 samples of the monzonitic granites are presented in Table 3. The monzonitic granite samples are characterized by high SiO₂ (68.62 wt.%–75.42 wt.%), high alkalinity (K₂O+Na₂O=6.51 wt.%–7.97 wt.%), high Na and low K, and the average K₂O/Na₂O ratio is 0.88. All of the samples fall into the sub-alkaline granite field in the TAS diagram of intrusive rocks (Fig. 7). The monzonitic granites present high Al₂O₃ (12.99 wt.%–15.45 wt.%), with A/CNK=0.99–1.14 and A/NK=1.48–1.87, and these results reflect the characteristics of peraluminous rock (Fig. 8). In addition, the high average FeO^T/MgO (4.15) ratio is also a feature of monzonitic granites. In the rock/chondritic, the values of the total REEs range of 83.12–151.51, which are obviously lower than those of the K-feldspar granites (Fig. 9). In general, the samples show an enrichment of LREEs (La_N/Yb_N=2.92–9.24; LREE/HREE: 4.17–9.24), stable

Table 2 Major, trace, and rare earth element data for the K-feldspar granites from Xilinhot area

Samples	HF0008-37	HF0008-62	HF0009-66	HF0007-1	HF0010-79	HF0008-42	HF0011-94	HF0441-5
Major element (wt.%)								
SiO ₂	74.77	75.32	75.49	75.77	75.85	76.13	76.66	72.94
TiO ₂	0.16	0.13	0.16	0.13	0.12	0.12	0.12	0.31
Al ₂ O ₃	13.3	13.01	12.88	13.17	13.03	12.7	13.08	13.97
Fe ₂ O ₃	0.81	0.82	0.8	0.6	0.59	0.69	0.16	0.84
FeO	0.9	0.94	0.97	0.68	0.67	0.78	0.2	0.92
FeO ^T	1.62	1.69	1.69	1.21	1.2	1.39	0.34	1.67
MnO	0.04	0.03	0.02	0.01	0.03	0.02	0.01	0.04
MgO	0.1	0.06	0.29	0.07	0.09	0.1	0.09	0.16
CaO	0.4	0.31	0.25	0.29	0.36	0.31	0.23	0.98
Na ₂ O	4.7	4.69	4.08	4.4	4.51	4.7	4.71	3.57
K ₂ O	3.92	3.65	3.78	3.99	3.87	3.7	3.95	5.4
P ₂ O ₅	0.03	0.02	0.02	0.02	0.02	0.02	0.02	0.05
H ₂ O ^T	0.54	0.65	0.89	0.58	0.57	0.45	0.5	0.5
H ₂ O ^C	0.41	0.35	0.76	0.44	0.34	0.39	0.44	0.08
F	0.02	0.02	0.02	0.02	0.04	0.01	0.02	0.03
CO ₂	0.06	0.08	0.1	0.06	0.08	0.06	0.1	0.11
Total	99.75	99.74	99.75	99.78	99.83	99.78	99.85	99.81
Trace element (ppm)								
Cs	12.16	5.48	15.01	14.88	11.48	6.09	5.03	8.09
Rb	119.8	109.6	122.2	149	140.8	114.2	125.2	178.4
Sr	60.3	39.4	57.9	47.6	31.5	50.2	36.5	80.6
Ba	458	404	424	334	348	350	367	611
Ga	21.9	23.1	19.6	19.3	20	21.4	20	22.8
Nb	7.11	6.89	7.13	5.88	5.32	5.66	5.66	17.35
Ta	0.71	0.62	0.66	0.68	0.57	0.63	0.63	1.52
Zr	254.6	263.5	296.3	190.4	189.2	199.9	181.3	412.4
Hf	7.9	7	8.6	6.4	6.2	6.1	6	11.2
Th	4.86	9.01	9.04	11.18	5.28	8.39	10.39	17.54
V	8.9	7.8	12.8	12.3	8	8.8	4.1	7.2
Cr	2.7	2.9	4.9	2.6	3.9	4	2.3	2.4
Be	2.3	2.56	1.78	2.29	2.61	2.5	2.08	2.82
Sn	9.73	4.95	5.18	3.95	7.58	7.01	5.56	9.1
Co	2.1	0.9	1.4	1.8	1.1	1.4	0.9	2.1
Ni	2.8	2.1	2.5	2.9	2.7	2.5	2.6	0.9
B	22.64	13.16	21.35	38.48	17.53	4.36	9.86	14.59
U	1.02	2.14	1.92	2	2.05	1.61	3.86	3.29
Rare earth element (ppm)								
La	17.34	25.95	19.17	23.54	17.93	19.38	19.13	37.88
Ce	49.56	57.55	36.04	49.9	49.91	54.65	48.32	72.99
Pr	5.75	7.93	6.2	6.46	5.51	6.4	5.4	10.08
Nd	22.1	31.75	25.03	24.23	20.92	25.63	20.65	37.79
Sm	5.24	7.58	5.46	5.25	4.86	6.01	4.57	7.22
Eu	0.77	0.81	0.75	0.52	0.5	0.65	0.51	1.16
Gd	5.14	8.16	5.42	5.54	4.78	5.97	4.88	5.7
Tb	0.93	1.39	0.97	0.92	0.88	1.07	0.85	0.85
Dy	5.85	8.48	5.98	5.59	5.44	6.52	5.48	4.83
Ho	1.3	1.82	1.33	1.22	1.2	1.41	1.17	0.85
Er	3.8	5.1	3.85	3.65	3.58	4.11	3.41	2.7
Tm	0.63	0.81	0.64	0.59	0.6	0.68	0.57	0.43
Yb	4.04	5.09	4.3	3.85	4.02	4.36	3.89	2.85
Lu	0.63	0.77	0.66	0.62	0.62	0.66	0.6	0.42
Y	30.48	46	31.21	31.69	27.94	31.33	31.02	23.16
ΣREE	123.08	163.19	115.8	131.88	120.75	137.5	119.43	185.75
La _N /Yb _N	3.08	3.66	3.2	4.39	3.2	3.19	3.53	9.53
LREE/HREE	4.51	4.16	4	5	4.72	4.55	4.73	8.97
δEu	0.45	0.31	0.42	0.29	0.31	0.33	0.33	0.53

Table 3 Major, trace, and rare earth element data for the monzonitic granites from Xilinhot area

Samples	HF0032-38	HF0007-13	HF0019-29	HF0008-48	HF0101-1	HF0101-8	HF0103-29	HF0101-10
Major element (wt.%)								
SiO ₂	74.69	68.62	68.67	74.67	71.69	72	72.32	73.54
TiO ₂	0.22	0.42	0.49	0.17	0.33	0.31	0.26	0.26
Al ₂ O ₃	13.15	15.45	15.03	13.49	14.26	14.02	13.8	13.82
Fe ₂ O ₃	0.6	1.11	1.12	0.71	0.99	0.96	0.65	0.66
FeO	1.12	1.6	2.22	0.79	1.47	1.3	1.47	0.86
FeO ^T	1.66	2.6	3.23	1.44	2.36	2.16	2.05	1.46
MnO	0.04	0.06	0.06	0.03	0.06	0.06	0.05	0.05
MgO	0.39	1.45	0.95	0.1	0.92	0.88	0.96	0.68
CaO	1.54	1.3	2.35	0.46	2.67	1.94	1.37	1.56
Na ₂ O	4.03	4.45	4.59	5.11	3.44	3.45	3.59	3.59
K ₂ O	3.58	3.52	2.9	3.56	3.1	3.58	3.83	3.63
P ₂ O ₅	0.04	0.1	0.11	0.02	0.08	0.08	0.07	0.06
H ₂ O ⁺	0.38	1.58	1.24	0.52	0.72	1.13	1.17	0.89
H ₂ O ⁻	0.21	0.73	0.47	0.43	0.25	0.37	0.41	0.42
F	0.032 87	0.021 7	0.030 38	0.019 11	0.033 54	0.030 23	0.023 14	0.030 63
CO ₂	0.04	0.12	0.08	0.12	0.06	0.08	0.29	0.21
Total	99.85	99.8	99.84	99.78	99.82	99.82	99.85	99.84
Trace element (ppm)								
Cs	3.64	22.83	2.99	16.6	1.84	1.53	10.83	1.47
Rb	111.4	111.9	96.3	114.6	66.4	73.3	118.6	72.3
Sr	98	446.3	159.3	55.1	251.7	229.4	230.7	222.3
Ba	404	553	369	406	661	555	366	524
Ga	17.4	15.7	21.7	24.2	15.7	16.3	15	15.4
Nb	5.61	4.87	5.66	7.06	6.14	7.44	7.18	10.45
Ta	0.52	0.5	0.64	0.8	0.49	0.62	0.91	1.23
Zr	147.3	162.2	247.1	299.4	117.4	112.5	94.9	91.8
Hf	4.2	5.5	6.8	8.5	3.6	3.8	3.3	2.6
Th	9.92	6.01	6.85	10.24	5.18	5.17	13.27	3.45
V	11.6	42.1	32.6	9	45.4	37.9	32.8	28.3
Cr	5.4	20	11.4	4.1	8.1	5.6	8.5	5.6
Co	2.7	7.2	6	1.8	5.4	4.7	4.1	3
Ni	3.6	6.8	7.2	3.5	4.4	4.2	4.5	4.1
B	3.68	22.5	5.5	12.96	4.81	10.79	20.75	13.99
U	1.11	1.64	2.88	2.09	0.62	0.71	2.17	0.88
Rare earth element (ppm)								
La	21.63	17.7	17.91	22.66	20.35	19.24	18.03	13.33
Ce	48.68	33.81	38.69	60.54	44.83	42.84	33.66	35.93
Pr	4.88	4.69	5.04	6.83	4.7	4.83	3.89	5.12
Nd	16.11	17.71	20.54	27.31	17.42	18.44	13.8	21.31
Sm	3.2	3.77	4.75	6.29	3.58	3.92	2.71	4.82
Eu	0.7	0.81	0.97	0.9	0.87	0.89	0.64	0.89
Gd	3.09	3.7	5.07	6.29	3.45	3.77	2.69	5.04
Tb	0.53	0.57	0.83	1.11	0.56	0.6	0.43	0.86
Dy	2.97	3.24	4.96	6.88	3.12	3.58	2.62	5.03
Ho	0.63	0.69	1.03	1.51	0.65	0.76	0.56	1.1
Er	1.8	1.94	3.05	4.52	1.83	2.14	1.64	3.21
Tm	0.28	0.31	0.49	0.77	0.28	0.34	0.27	0.52
Yb	1.68	1.97	3.11	5.1	1.7	1.98	1.87	3.28
Lu	0.26	0.31	0.49	0.8	0.25	0.29	0.31	0.49
Y	16.45	18.26	27.24	35.26	17.08	20.03	15.49	29.67
ΣREE	106.44	91.22	106.93	151.51	103.59	103.62	83.12	100.93
La _N /Yb _N	9.24	6.44	4.13	3.19	8.59	6.97	6.92	2.92
LREE/HREE	8.47	6.17	4.62	4.62	7.75	6.7	7	4.17
δEu	0.67	0.65	0.6	0.43	0.75	0.7	0.72	0.55

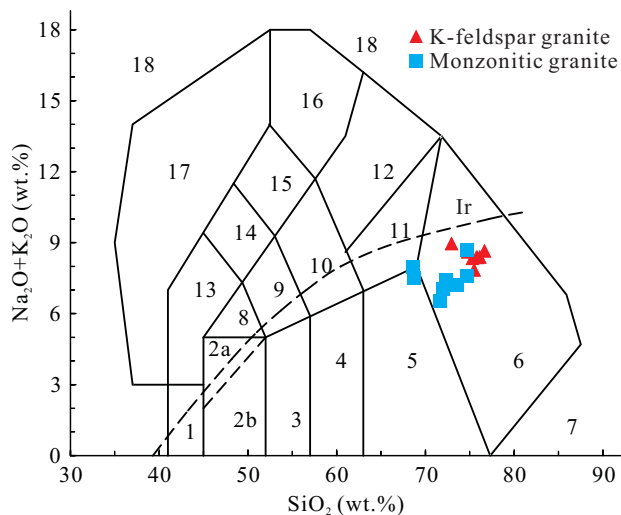


Figure 7. Alkali-silica classification diagram (TAS; wt.%) (Middlemost, 1994) for the two genetic types of granites from Xilinhot. Ir. Irvine line.

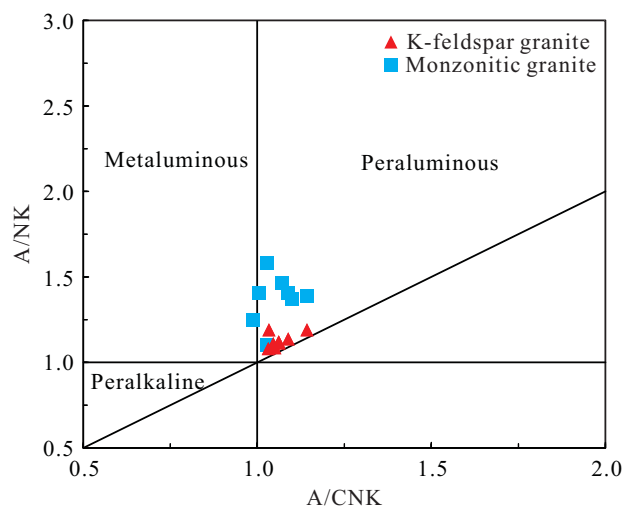


Figure 8. A/NK [molar ratio $\text{Al}_2\text{O}_3/(\text{Na}_2\text{O} + \text{K}_2\text{O})$] vs. A/CNK [molar ratio $\text{Al}_2\text{O}_3/(\text{CaO} + \text{Na}_2\text{O} + \text{K}_2\text{O})$] diagram (Maniar and Piccoli, 1989) for the two genetic types of granites from Xilinhot.

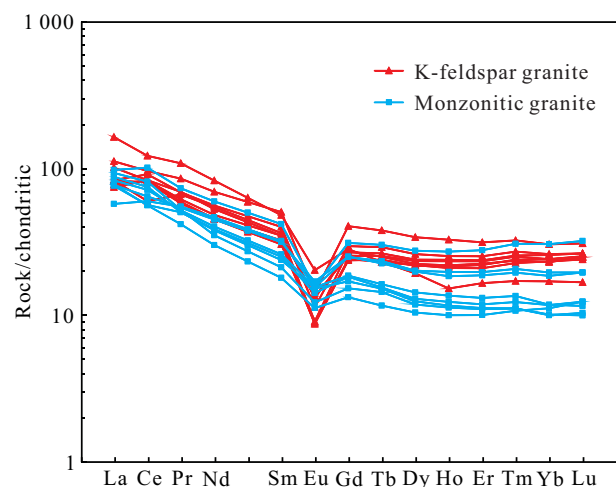


Figure 9. Chondrite-normalized REE distribution patterns for the two genetic types of granites from Xilinhot. Normalization values are from Sun and McDonough (1989).

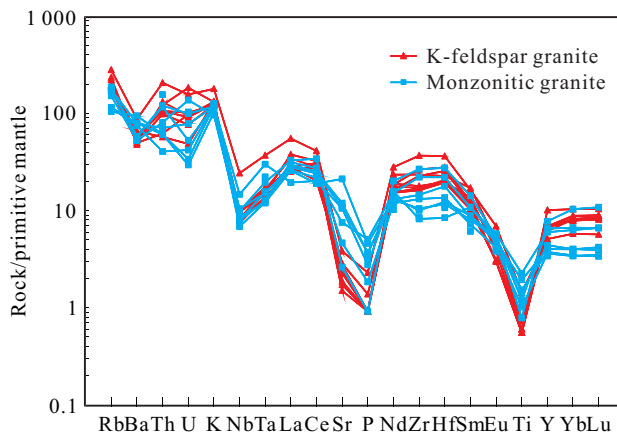


Figure 10. Primitive mantle-normalized trace element spidergrams for the two genetic types of granites from Xilinhot. Normalization values are from Sun and McDonough (1989).

amounts of HREEs, and negative Eu anomalies ($\delta\text{Eu}=0.43\text{--}0.75$); however, the degree of enrichment is obviously less than that of the K-feldspar granites. For the trace elements (Fig. 10), the monzonitic granites display a distinct enrichment of LILE (K, Rb, Ba) and HFSE (Zr, Hf) but show obvious negative abnormalities of the Nb, Ta, Sr, P and Ti elements. The degree of the negative abnormality for the Ti element is less than that of the K-feldspar granites.

3.3 Zircon Lu-Hf Data

Table 4 presents the Lu-Hf isotope analysis of the two genetic types of granites in Xilinhot. The initial $^{176}\text{Hf}/^{177}\text{Hf}$ ratio of the K-feldspar granites is relatively high and ranges of 0.282 930–0.282 980, and the values of $\epsilon_{\text{Hf}}(t)$ are strongly positive (Fig. 11) and range from +5.4 to +10.7, with a mean value of +13.6. The two-stage model ages ($T_{\text{DM}2}$) range of 420–503 Ma, with an average age of 453 Ma.

In contrast, the initial $^{176}\text{Hf}/^{177}\text{Hf}$ ratio of the monzonitic granites ranges of 0.282 719–0.282 878 and is obviously lower than that of the K-feldspar granites; however, the monzonitic granite samples present a positive $\epsilon_{\text{Hf}}(t)$ that ranges from +5.4 to +10.7 (Fig. 11) and a mean value of +7.4. These values are distinctly lower than that of the K-feldspar granites except for the $T_{\text{DM}2}$ value, which ranges from 615 to 927 Ma and has an average age of 798 Ma.

4 DISCUSSION

4.1 Petrogenesis

The two genetic types of granites in the Xilinhot area of Inner Mongolia display a distinct relationship in which they act as intrusions and include intrusions. The 9 Ma interval of these two plutons and the younger intrusion age of the more acidic pluton (the K-feldspar granites) indicate that the two genetic types of granites may not have formed from the fractional crystallization of the same batch magma and suggest that they belong to different batches from the same magma origin region or were formed from diverse magmatic sources.

The chondrite-normalized REE distribution patterns (Fig. 9) were compared with the primitive mantle-normalized trace element spidergrams of the two genetic types of granites (Fig. 10), and the higher value of the total REEs and the more negative

Table 4 Zircon Lu-Hf isotope data for the two types granites in Xilinhot area

Samples	Spots	Age (Ma)	$^{176}\text{Hf}/^{177}\text{Hf}$	$^{176}\text{Lu}/^{177}\text{Hf}$	$^{176}\text{Lu}/^{177}\text{Hf}$	$^{176}\text{Yb}/^{177}\text{Hf}$	1σ	Age (Ma)	$\epsilon_{\text{Hf}}(0)$	1σ	$\epsilon_{\text{Hf}}(t)$	1σ	T_{DM1} (Ma)	T_{DM2} (Ma)	f_{LuHf}
K-feldspar granite	0024-9-01	338	0.282 98	0.000 009	0.002 549	0.000 013	0.077 727	338	7.4	0.6	14.2	0.6	402	423	-0.92
	0024-9-02	339	0.282 944	0.000 007	0.001 16	0.000 025	0.034 675	339	6.1	0.6	13.3	0.6	438	476	-0.97
	0024-9-03	324	0.282 964	0.000 008	0.001 262	0.000 043	0.038 779	324	6.8	0.6	13.7	0.6	411	444	-0.96
	0024-9-04	331	0.282 964	0.000 009	0.001 819	0.000 026	0.052 548	331	6.8	0.6	13.7	0.6	417	448	-0.95
	0024-9-05	337	0.282 93	0.000 01	0.000 986	0.000 07	0.027 582	337	5.6	0.6	12.8	0.7	456	503	-0.97
	0024-9-06	330	0.282 971	0.000 011	0.001 877	0.000 064	0.057 071	330	7	0.6	13.9	0.7	407	436	-0.94
	0024-9-07	331	0.282 95	0.000 009	0.001 708	0.000 009	0.050 858	331	6.3	0.6	13.2	0.6	437	476	-0.95
	0024-9-08	331	0.282 976	0.000 008	0.001 445	0.000 01	0.044 899	331	7.2	0.6	14.2	0.6	395	420	-0.96
Monzonitic granite	0102-17-01	323	0.282 807	0.000 011	0.001 818	0.000 026	0.057 91	323	1.3	0.6	8	0.7	644	761	1.3
	0102-17-02	353	0.282 719	0.000 009	0.001 993	0.000 023	0.064 514	353	-1.9	0.6	5.4	0.6	776	927	-1.9
	0102-17-03	327	0.282 781	0.000 009	0.001 986	0.000 036	0.062 144	327	0.3	0.6	7.1	0.6	685	813	0.3
	0102-17-04	320	0.282 779	0.000 01	0.001 411	0.000 055	0.043 905	320	0.3	0.6	7	0.6	677	813	0.3
	0102-17-05	323	0.282 772	0.000 009	0.001 567	0.000 006	0.047 747	323	0	0.6	6.8	0.6	690	827	0
	0102-17-06	329	0.282 878	0.000 013	0.001 504	0.000 104	0.043 554	329	3.8	0.7	10.7	0.7	537	615	3.8
	0102-17-07	327	0.282 815	0.000 012	0.001 684	0.000 044	0.048 144	327	1.5	0.7	8.3	0.7	631	744	1.5
	0102-17-08	321	0.282 741	0.000 014	0.001 248	0.000 043	0.037 62	321	-1.1	0.7	5.7	0.7	729	886	-1.1

$\epsilon_{\text{Hf}}(t) = 10 \times \{ [(^{176}\text{Hf}/^{177}\text{Hf})_{\text{sample}} / (^{176}\text{Lu}/^{177}\text{Hf})_{\text{sample}} \times (e^{-\lambda t}) / ((^{176}\text{Hf}/^{177}\text{Hf})_{\text{DM}} \times (e^{-\lambda t}) - 1)] - 1 \}$; $T_{\text{DM1}} = 1 / \ln \{ 1 + [(^{176}\text{Hf}/^{177}\text{Hf})_{\text{sample}} / (^{176}\text{Lu}/^{177}\text{Hf})_{\text{DM}}] / [(^{176}\text{Lu}/^{177}\text{Hf})_{\text{DM}} - (^{176}\text{Lu}/^{177}\text{Hf})_{\text{sample}}] \}$; $T_{\text{DM2}} = T_{\text{DM1}} - (T_{\text{DM1}} - t) \times [(c_{\text{cc}} - f_{\text{DM}}) / (c_{\text{cc}} - f_{\text{DM}})]$; $f_{\text{LuHf}} = (^{176}\text{Lu}/^{177}\text{Hf})_{\text{sample}} / (^{176}\text{Lu}/^{177}\text{Hf})_{\text{CHUR}} - 1$; $\lambda = 1.876 \times 10^{-11} \text{ a}^{-1}$ (Söderlund et al., 2004); $(^{176}\text{Lu}/^{177}\text{Hf})_{\text{s}}$ and $(^{176}\text{Lu}/^{177}\text{Hf})_{\text{DM}}$ as the measured values of sample; $(^{176}\text{Lu}/^{177}\text{Hf})_{\text{CHUR}} = 0.033 2$, $(^{176}\text{Hf}/^{177}\text{Hf})_{\text{CHUR}} = 0.282 772$ (Blichert-Toft and Albarède, 1997); $(^{176}\text{Lu}/^{177}\text{Hf})_{\text{DM}} = 0.038 4$, $(^{176}\text{Hf}/^{177}\text{Hf})_{\text{DM}} = 0.283 25$ (Griffin et al., 2000); $f_{\text{cc}} = [(^{176}\text{Lu}/^{177}\text{Hf})_{\text{DM}} / (^{176}\text{Lu}/^{177}\text{Hf})_{\text{CHUR}}] - 1$; $f_{\text{LuHf}} = [(^{176}\text{Lu}/^{177}\text{Hf})_{\text{DM}} / (^{176}\text{Lu}/^{177}\text{Hf})_{\text{CHUR}}] - 1$.

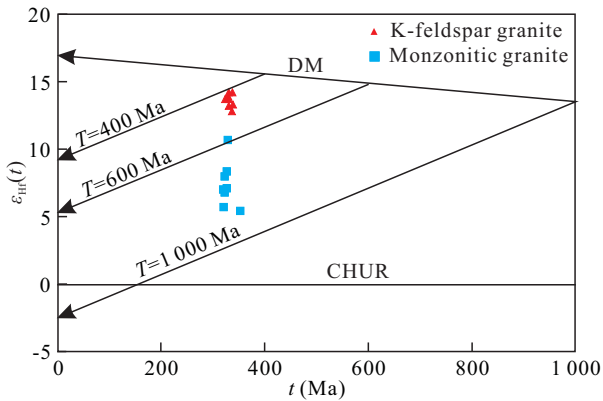


Figure 11. Zircon Hf isotopic features for the two genetic types of granites in the Xilinhot area.

anomalies of Sr and Eu in the K-feldspar granites indicate that a lower degree of partial melting occurred at the magmatic source, where the plagioclase may be remnant. Thus, the K-feldspar granites could not have been derived from mantle sources (in extreme conditions, strong crystal fractionation of mantle magma can generate alkaline rocks with limited or low Sr and Eu elements; however, massive mafic rocks would be observed). In addition, both of the granites present negative anomalies of Ti, P and Nb elements, which may have been caused by the remnants of rutile, apatite, or other accessory minerals in the lower crust source region or by the occurrence of fractional crystallization of accessory minerals during the rising stage of the magma.

To distinguish the A-type granite from other types of granites, the diagrams of Whalen et al. (1987) are widely used. All of the samples of the K-feldspar granites are characterized by high values of $10^4 \times \text{Ga}/\text{Al}$ and an average value of 3.02, and they fall in the field of A-type granite (Fig. 12). Because of their high alkali contents, elevated Fe/Mg and Ga/Al, low abundance of Ba and Sr, and high concentrations of Zr, Nb, these granites are exclusively distributed into the A-type field in the discrimination diagrams of Whalen et al. (1987). Furthermore, the K-feldspar granites are ferroan, alkali and peraluminous in terms of the A-type granitoid classification scheme of Frost et al. (2001). In contrast, 6 of the 8 samples of the monzonitic granites fall into the non-A-type granite field. Moreover, based on the concentrations that falls in the A2 field on the Nb-Y-Ga (Fig. 13a) and Nb-Y-Ce diagrams (Fig. 13b) (Eby, 1992) and the PA field on the $R1-10^4 \times \text{Ga}/\text{Al}$ diagram (Fig. 13c), the Xilinhot K-feldspar granites exhibit a post-orogenic extensional tectonic setting. In the R1-R2 multicationic scheme (Batchelor and Bowden, 1985), the K-feldspar granites are concentrated in the field of a post-orogenic setting (Fig. 14), although the monzonitic granites fall in the region of a syn-collision. The results cannot be interpreted to show that the monzonitic granites are formed with the tectonic setting of syn-collision; rather, the results indicate that they occurred as a hybridization of crust materials before the magma emplacement.

The distinct degree of compatibility between the Lu and Hf elements in the zircons causes the enrichment of the Hf element, and the lack of Lu element causes the zircons to always have a low ratio of Lu/Hf. Thus, radiogenic Hf is scarcely produced during the decay process of the Lu element; moreover, the high seal-

ing temperature and the strong ability to resist the reformation of the hydrothermal fluids indicate that the measured ratio of $^{176}\text{Hf}/^{177}\text{Hf}$ can represent the Hf isotope composition during the formation of the isotopic system (Wu et al., 2007; Kinny and Maas, 2003). Studying the isotope system of Hf represents a reasonable method of tracing the origin of the magma. The ionic radius and electrovalence of Lu allow this element to stay in the magmatic residual phase, which is inconsistent with the characteristics of Hf during the process of partial melting. The $\epsilon_{\text{Hf}}(t)$ values indicate that the juvenile crust and residual mantle evolved toward different directions (the juvenile crust moves toward negative values, and the residual mantle moves toward positive values), and the zircon Hf isotope composition can be used to provide information on the magmatic source.

Most granites are considered to have originated from crustal sources. If the two-stage model age (T_{DM2}) is much larger than the emplacement age, then the granites might have formed by crustal melting. If the T_{DM2} is close to the emplacement age, then the granites might have formed from the juvenile crust. Although both granites show positive zircon $\epsilon_{\text{Hf}}(t)$ values, significant differences were observed in the zircon Hf isotope composition between the two genetic types of granites. The earlier emplaced K-feldspar granites (332 Ma) have a higher $\epsilon_{\text{Hf}}(t)$ value than the centralized younger T_{DM2} granites (453 Ma) (Fig. 11). However, the later emplaced monzonite granites (323 Ma) present lower $\epsilon_{\text{Hf}}(t)$ values and older separate T_{DM2} ages (798 Ma) (Fig. 11). A strongly positive $\epsilon_{\text{Hf}}(t)$ value and young T_{DM2} indicates that the Xilinhot area may have been formed in the Early Paleozoic as a juvenile lower crust. The dispersed age of the monzonite granites and the older average T_{DM2} (798 Ma) reflect that a different degree of contamination occurred in the older continental crust above the juvenile lower crust.

4.2 Tectonic Evolution

It is still uncertain when the Paleo-Asian Ocean closed. The Baolidao island-arc type granite series (414–418 Ma) and the Bayanhalatu collision granite series (363 Ma) are closely related to the subduction and collision process of the Paleo-Asian Ocean (Chen and Xu, 1996). On a regional scale, the Devonian–Early Carboniferous molasses and the epi-continental carbonate deposits do not uniformly overlie an imbricated oceanic rock suite bordering the suture zone (Tang, 1990). In addition, an unconformable surface occurs under the Upper Devonian Seribayanaobao Group (Shao et al., 2015). The lower part is a greenschist series with medium pressure orogenic metamorphism, and the upper part is generally non-metamorphic and has thick-bedded basal conglomerate. This evidence indicates that the subduction of the Paleo-Asian Ocean was not complete until at least the Late Devonian and suggests that collision and orogeny had already started at this point. The Xilinhot K-feldspar granites with representative post-orogenic A-type granite characteristics indicate that the region represents a post-orogenic extension stage. During the Late Devonian–Early Carboniferous, the collision and orogeny were complete and the subduction slab broke off, and these changes led to the thermal upwelling of the asthenosphere and the resulting lithospheric extension and melting of the juvenile crust, which formed during the oceanic subduction. In addition, the rising magma was contaminated by the overlying

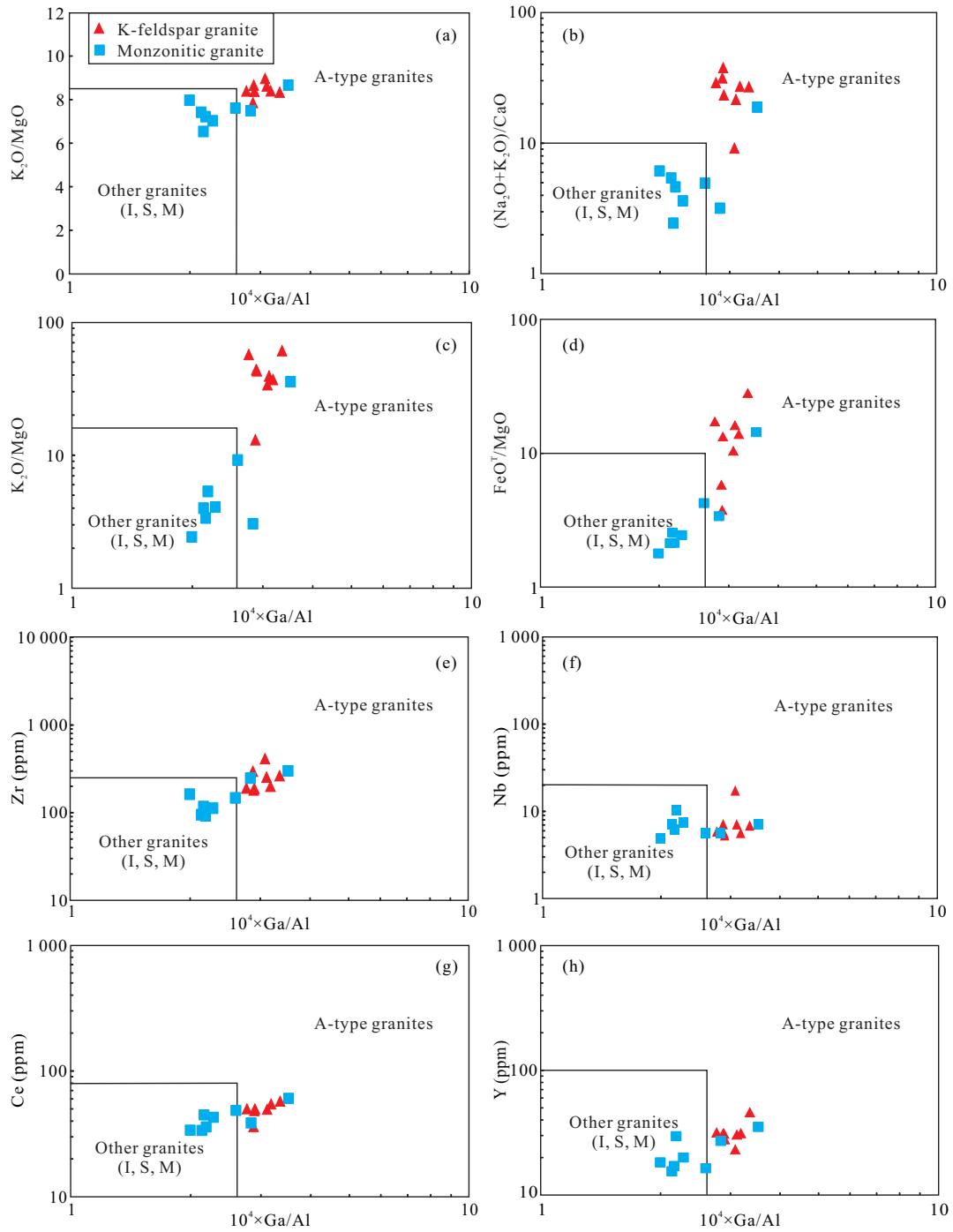


Figure 12. A-type granite geochemical discrimination diagrams of Whalen et al. (1987).

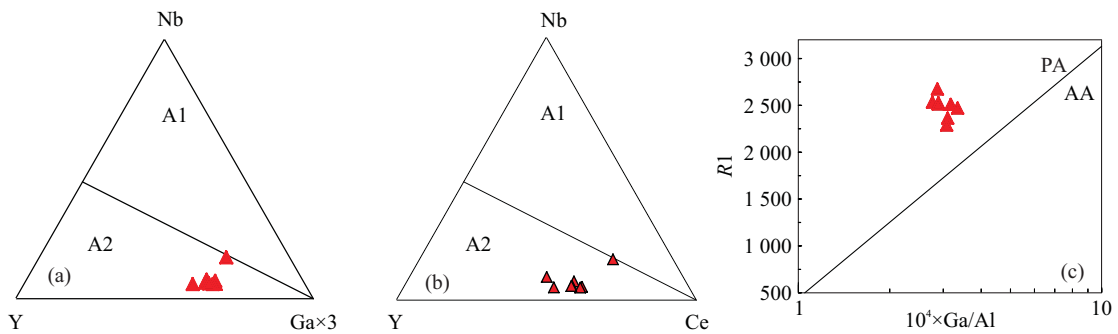


Figure 13. (a) Nb-Y-Ga ternary diagram and (b) Nb-Y-Ce ternary diagram (after Eby, 1992); (c) $R1 (=4Si-11(Na+K)-2(Fe+Ti))$ vs. $10^4 \times Ga/Al$ diagram (after Hong et al., 1995). All of the samples are K-feldspar granites.

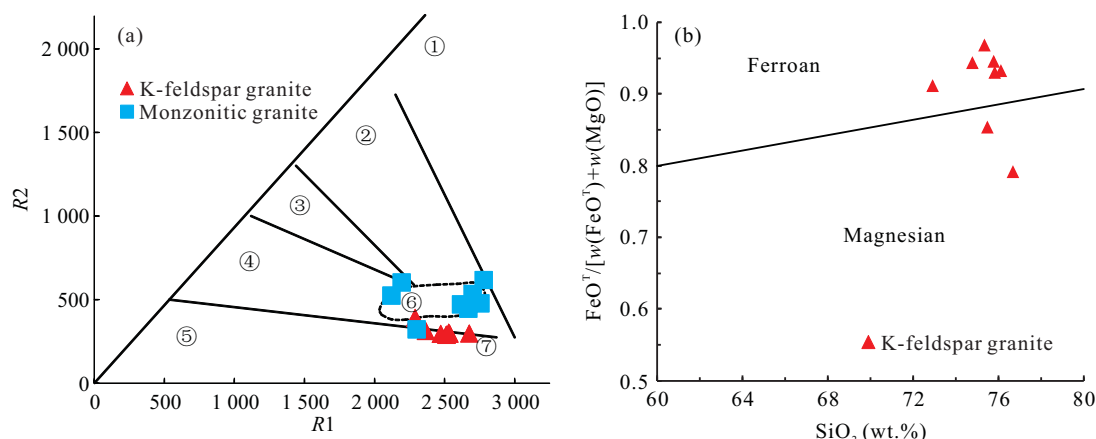


Figure 14. (a) $R2$ ($=6Ca+2Mg+Al$) vs. $R1$ ($=4Si-11(Na+K)-2(Fe+Ti)$) diagram (after Batchelor and Bowden, 1985).

ancient crustal material. The coetaneous ultrabasic-basic rocks (354–333 Ma) with high $\varepsilon_{Nd}(t)$ values (Jian et al., 2012) in the Xiaobaliang area and the gabbros (319 Ma) (Zhou et al., 2016) with high $\varepsilon_{Hf}(t)$ values in the Xilinhot area also support the asthenosphere upwelling and melting of the juvenile crust.

Recent studies on sedimentation and paleo-magnetic reconstructions (Zhao et al., 2013) demonstrate that the inland sea developed on a welded continent after the collision between the North China Plate and the northern blocks during the Late Carboniferous Period (Zhao et al., 2016).

5 CONCLUSIONS

(1) The U-Pb ages indicate that the two species of granite are Lower Carboniferous, with the K-feldspar granite emplacing at 332 Ma and showing typical A-type granite geochemical characteristics in the post-collision stage, and the emplacement age of the monzonite granite is 323 Ma.

(2) The two granites reveal higher $\varepsilon_{Hf}(t)$ values, with the K-feldspar granite at 13.6 and the monzonite granite at 7.4 on average. The two-stage model ages of these granites are 453 and 798 Ma. These Hf isotope features reflect that the magma originated from the partial melting of the juvenile crust, and the monzonite granite was derived from mantle contaminated by ancient crustal material.

(3) The above results indicate a more recent post-orogenic period and demonstrate that the Paleo-Asian Ocean had closed before the Early Carboniferous Period, and they show that the Xilinhot area experienced its initial post-orogenic evolution in an extensional tectonic environment in the Early Carboniferous Period.

ACKNOWLEDGMENTS

The authors are indebted to Prof. Defan Xie from the School of Earth Sciences, China University of Geosciences, Wuhan for his guidance during field work, and thanks also go to Jianzhen Geng and Yongqing Zhang for the zircon U-Pb dating by LA-ICP-MS at the Tianjin Center of China Geological Survey. This study was supported by the China Geological Survey (Nos. 1212010510507, 1212010811005, 1212011220448) and the Fundamental Research Funds for the Central Universities, China University of Geosciences, Wuhan (No. CUGL150816). The final publication is available at Springer via <https://doi.org/10.1007/s12583-017-0942-2>.

REFERENCES CITED

- Andersen, T., 2002. Correction of Common Lead in U-Pb Analyses that do not Report ^{204}Pb . *Chemical Geology*, 192(1/2): 59–79. [https://doi.org/10.1016/s0009-2541\(02\)00195-x](https://doi.org/10.1016/s0009-2541(02)00195-x)
- Badarch, G., Cunningham, W. D., Windley, B. F., 2002. A New Terrane Subdivision for Mongolia: Implications for the Phanerozoic Crustal Growth of Central Asia. *Journal of Asian Earth Sciences*, 21(1): 87–110. [https://doi.org/10.1016/s1367-9120\(02\)00017-2](https://doi.org/10.1016/s1367-9120(02)00017-2)
- Batchelor, R. A., Bowden, P., 1985. Petrogenetic Interpretation of Granitoid Rock Series Using Multicationic Parameters. *Chemical Geology*, 48(1/2/3/4): 43–55. [https://doi.org/10.1016/0009-2541\(85\)90034-8](https://doi.org/10.1016/0009-2541(85)90034-8)
- Blichert-Toft, J., Albarède, F., 1997. The Lu-Hf Isotope Geochemistry of Chondrites and the Evolution of the Mantle-Crust System. *Earth and Planetary Science Letters*, 148(1/2): 243–258. [https://doi.org/10.1016/s0012-821x\(97\)00040-x](https://doi.org/10.1016/s0012-821x(97)00040-x)
- Buslov, M. M., Fujiwara, Y., Iwata, K., et al., 2004. Late Paleozoic–Early Mesozoic Geodynamics of Central Asia. *Gondwana Research*, 7(3): 791–808. [https://doi.org/10.1016/s1342-937x\(05\)71064-9](https://doi.org/10.1016/s1342-937x(05)71064-9)
- Chen, B., Xu, B., 1996. The Main Characteristics and Tectonic Implications of Two Kinds of Paleozoic Granitoids in Sunidzuqi, Central Inner Mongolia. *Acta Petrologica Sinica*, 10(4): 49–64 (in Chinese with English Abstract)
- Demoux, A., Kröner, A., Badarch, G., et al., 2009. Zircon Ages from the Baydrag Block and the Bayankhongor Ophiolite Zone: Time Constraints on Late Neoproterozoic to Cambrian Subduction- and Accretion-Related Magmatism in Central Mongolia. *The Journal of Geology*, 117(4): 377–397. <https://doi.org/10.1086/598947>
- Eby, G. N., 1992. Chemical Subdivision of the A-Type Granitoids: Petrogenetic and Tectonic Implications. *Geology*, 20(7): 641–644. [https://doi.org/10.1130/0091-7613\(1992\)020<0641:csotat>2.3.co;2](https://doi.org/10.1130/0091-7613(1992)020<0641:csotat>2.3.co;2)
- Frost, B. R., Barnes, C. G., Collins, W. J., et al., 2001. A Geochemical Classification for Granitic Rocks. *Journal of Petrology*, 42(11): 2033–2048. <https://doi.org/10.1093/petrology/42.11.2033>
- Glorie, S., De Grave, J., Buslov, M. M., et al., 2011. Formation and Palaeozoic Evolution of the Gorny-Altai–Altai-Mongolia Suture Zone (South Siberia): Zircon U/Pb Constraints on the Igneous Record. *Gondwana Research*, 20(2/3): 465–484. <https://doi.org/10.1016/j.gr.2011.03.003>
- Griffin, W. L., Pearson, N. J., Belousova, E., et al., 2000. The Hf Isotope Composition of Cratonic Mantle: LAM-MC-ICPMS Analysis of Zircon Megacrysts in Kimberlites. *Geochimica et Cosmochimica Acta*, 64(1): 133–147. [https://doi.org/10.1016/s0016-7037\(99\)00343-9](https://doi.org/10.1016/s0016-7037(99)00343-9)
- Han, B. F., He, G. Q., Wang, X. C., et al., 2011. Late Carboniferous Collision between the Tarim and Kazakhstan-Yili Terranes in the Western

- Segment of the South Tian Shan Orogen, Central Asia, and Implications for the Northern Xinjiang, Western China. *Earth-Science Reviews*, 109(3/4): 74–93. <https://doi.org/10.1016/j.earscirev.2011.09.001>
- Han, B. F., Wang, S. G., Jahn, B. M., et al., 1997. Depleted-Mantle Source for the Ulungur River A-Type Granites from North Xinjiang, China: Geochemistry and Nd-Sr Isotopic Evidence, and Implications for Phanerozoic Crustal Growth. *Chemical Geology*, 138(3/4): 135–159. [https://doi.org/10.1016/s0009-2541\(97\)00003-x](https://doi.org/10.1016/s0009-2541(97)00003-x)
- Hong, D. W., Huang, H. Z., Xiao, Y. J., 1994. The Permian Alkaline Granites in Central Inner Mongolia and Their Geodynamic Significance. *Acta Geologica Sinica*, 10(3): 219–230 (in Chinese with English Abstract)
- Hong, D. W., Wang, S. G., Han, B. F., et al., 1995. Tectonic Environment Classification and Identifying Symbol of Alkali Granite. *Science in China (Series B)*, 25(4): 418–426 (in Chinese)
- Hong, D. W., Zhang, J. S., Wang, T., et al., 2004. Continental Crustal Growth and the Supercontinental Cycle: Evidence from the Central Asian Orogenic Belt. *Journal of Asian Earth Sciences*, 23(5): 799–813. [https://doi.org/10.1016/s1367-9120\(03\)00134-2](https://doi.org/10.1016/s1367-9120(03)00134-2)
- Hsu, K. J., Wang, Q. C., Li, L., et al., 1991. Geologic Evolution of the Neimonides: A Working Hypothesis. *Eclogae Geologicae Helveticae*, 84(1): 1–31
- Hu, Z. C., Liu, Y. S., Gao, S., et al., 2008a. A Local Aerosol Extraction Strategy for the Determination of the Aerosol Composition in Laser Ablation Inductively Coupled Plasma Mass Spectrometry. *Journal of Analytical Atomic Spectrometry*, 23(9): 1192–1203. <https://doi.org/10.1039/b803934h>
- Hu, Z. C., Gao, S., Liu, Y. S., et al., 2008b. Signal Enhancement in Laser Ablation ICP-MS by Addition of Nitrogen in the Central Channel Gas. *Journal of Analytical Atomic Spectrometry*, 23(8): 1093–1101. <https://doi.org/10.1039/b804760j>
- Hu, Z. C., Liu, Y. S., Gao, S., et al., 2012. Improved *in situ* Hf Isotope Ratio Analysis of Zircon Using Newly Designed X Skimmer Cone and Jet Sample Cone in Combination with the Addition of Nitrogen by Laser Ablation Multiple Collector ICP-MS. *Journal of Analytical Atomic Spectrometry*, 27(9): 1391–1399. <https://doi.org/10.1039/c2ja30078h>
- Jahn, B. M., Litvinovsky, B. A., Zanzvilevich, A. N., et al., 2009. Peralkaline Granitoid Magmatism in the Mongolian-Transbaikalian Belt: Evolution, Petrogenesis and Tectonic Significance. *Lithos*, 113(3/4): 521–539. <https://doi.org/10.1016/j.lithos.2009.06.015>
- Jahn, B. M., Wu, F. Y., Chen, B., 2000a. Granitoids of the Central Asian Orogenic Belt and Continental Growth in the Phanerozoic. *Transactions of the Royal Society of Edinburgh: Earth Sciences*, 91(1/2): 181–193. <https://doi.org/10.1017/s0263593300007367>
- Jahn, B. M., Wu, F. Y., Chen, B., 2000b. Massive Granitoid Generation in Central Asia: Nd Isotope Evidence and Implication for Continental Growth in the Phanerozoic. *Episodes*, 23(2): 82–92
- Jian, P., Kröner, A., Windley, B. F., et al., 2012. Carboniferous and Cretaceous Mafic-Ultramafic Massifs in Inner Mongolia (China): A SHRIMP Zircon and Geochemical Study of the Previously Presumed Integral “Hegenshan Ophiolite”. *Lithos*, 142/143: 48–66. <https://doi.org/10.1016/j.lithos.2012.03.007>
- Jian, P., Liu, D. Y., Kröner, A., et al., 2008. Time Scale of an Early to Mid-Paleozoic Orogenic Cycle of the Long-Lived Central Asian Orogenic Belt, Inner Mongolia of China: Implications for Continental Growth. *Lithos*, 101(3/4): 233–259. <https://doi.org/10.1016/j.lithos.2007.07.005>
- Khain, E. V., Bibikova, E. V., Kröner, A., et al., 2002. The Most Ancient Ophiolite of the Central Asian Fold Belt: U-Pb and Pb-Pb Zircon Ages for the Dунzhugur Complex, Eastern Sayan, Siberia, and Geodynamic Implications. *Earth and Planetary Science Letters*, 199(3/4): 311–325. [https://doi.org/10.1016/s0012-821x\(02\)00587-3](https://doi.org/10.1016/s0012-821x(02)00587-3)
- Khain, E., Bibikova, E. V., Salmikova, E. B., et al., 2003. The Palaeo-Asian Ocean in the Neoproterozoic and Early Palaeozoic: New Geochronologic Data and Palaeotectonic Reconstructions. *Precambrian Research*, 122(1/2/3/4): 329–358. [https://doi.org/10.1016/s0301-9268\(02\)00218-8](https://doi.org/10.1016/s0301-9268(02)00218-8)
- Kinny, P. D., Maas, R., 2003. Lu-Hf and Sm-Nd Isotope Systems in Zircon. *Reviews in Mineralogy and Geochemistry*, 53(1): 327–341. <https://doi.org/10.2113/0530327>
- Kröner, A., Demoux, A., Zack, T., et al., 2011. Zircon Ages for a Felsic Volcanic Rock and Arc-Related Early Palaeozoic Sediments on the Margin of the Baydrag Microcontinent, Central Asian Orogenic Belt, Mongolia. *Journal of Asian Earth Sciences*, 42(5): 1008–1017. <https://doi.org/10.1016/j.jseae.2010.09.002>
- Kröner, A., Lehmann, J., Schulmann, K., et al., 2010. Lithostratigraphic and Geochronological Constraints on the Evolution of the Central Asian Orogenic Belt in SW Mongolia: Early Paleozoic Rifting Followed by Late Paleozoic Accretion. *American Journal of Science*, 310(7): 523–574. <https://doi.org/10.2475/07.2010.01>
- Kröner, A., Windley, B. F., Badarch, G., et al., 2007. Accretionary Growth and Crust Formation in the Central Asian Orogenic Belt and Comparison with the Arabian-Nubian Shield. *Geological Society of America Memoirs*, 200(5): 181–209
- Li, J. Y., 2006. Permian Geodynamic Setting of Northeast China and Adjacent Regions: Closure of the Paleo-Asian Ocean and Subduction of the Paleo-Pacific Plate. *Journal of Asian Earth Sciences*, 26(3/4): 207–224. <https://doi.org/10.1016/j.jseae.2005.09.001>
- Li, J. Y., Gao, L. M., Sun, G. H., et al., 2007. Shuangjingzi Middle Triassic Syn-Collisional Crust-Derived Granite in the East Inner Mongolia and Its Constraint on the Timing of Collision between Siberian and Sino-Korean Paleo-Plates. *Acta Petrologica Sinica*, 23(3): 565–582 (in Chinese with English Abstract)
- Liu, Y. S., Gao, S., Hu, Z. C., et al., 2009. Continental and Oceanic Crust Recycling-Induced Melt-Peridotite Interactions in the Trans-North China Orogen: U-Pb Dating, Hf Isotopes and Trace Elements in Zircons from Mantle Xenoliths. *Journal of Petrology*, 51(1/2): 537–571. <https://doi.org/10.1093/ptrology/egp082>
- Liu, Y. S., Hu, Z. C., Gao, S., et al., 2008. *In situ* Analysis of Major and Trace Elements of Anhydrous Minerals by LA-ICP-MS without Applying an Internal Standard. *Chemical Geology*, 257(1/2): 34–43. <https://doi.org/10.1016/j.chemgeo.2008.08.004>
- Ludwig, K. R., 2003. ISOPLOT 3.00: A Geochronological Toolkit for Microsoft Excel. Berkeley Geochronology Center, Berkeley
- Ma, S. W., Liu, C. F., Xu, Z. Q., et al., 2017. Geochronology, Geochemistry and Tectonic Significance of the Early Carboniferous Gabbro and Diorite Plutons in West Ujimqin, Inner Mongolia. *Journal of Earth Science*, 28(2): 249–264. <https://doi.org/10.1007/s12583-016-0912-2>
- Maniar, P. D., Piccoli, P. M., 1989. Tectonic Discrimination of Granitoids. *Geological Society of America Bulletin*, 101(5): 635–643. [https://doi.org/10.1130/0016-7606\(1989\)101<0635:tdog>2.3.co;2](https://doi.org/10.1130/0016-7606(1989)101<0635:tdog>2.3.co;2)
- Middlemost, E. A. K., 1994. Naming Materials in the Magma/Igneous Rock System. *Earth-Science Reviews*, 37(3/4): 215–224. [https://doi.org/10.1016/0012-8252\(94\)90029-9](https://doi.org/10.1016/0012-8252(94)90029-9)
- Möller, A., O'Brien, P. J., Kennedy, A., et al., 2003. Linking Growth Episodes of Zircon and Metamorphic Textures to Zircon Chemistry: An Example from the Ultrahigh-Temperature Granulites of Rogaland (SW Norway). *Geological Society, London, Special Publications*, 220(1): 65–81. <https://doi.org/10.1144/gsl.sp.2003.220.01.04>
- Mossakovsky, A. A., Ruzhentsev, S. V., Samygin, S. G., et al., 1994. Cen-

- tral Asian Fold Belt: Geodynamic Evolution and Formation History. *Geotectonics*, 27(6): 445–474
- Pearce, N. J. G., Perkins, W. T., Westgate, J. A., et al., 1997. A Compilation of New and Published Major and Trace Element Data for NIST SRM 610 and NIST SRM 612 Glass Reference Materials. *Geostandards and Geoanalytical Research*, 21(1): 115–144. <https://doi.org/10.1111/j.1751-908x.1997.tb00538.x>
- Rubatto, D., Gebauer, D., 2000. Use of Cathodoluminescence for U-Pb Zircon Dating by Ion Microprobe: Some Examples from the Western Alps. In: Pagel, M., Barbin, V., Blanc, P., et al., eds., *Cathodoluminescence in Geosciences*. Springer-Verlag Berlin Heidelberg, [S.l.]. 373–400
- Şengör, A. M. C., Natal'in, B. A., 1996. Paleotectonics of Asia: Fragments of a Synthesis. In: Yin, A., Harrison, M., eds., *The Tectonic Evolution of Asia*. Cambridge University Press, Cambridge. 486–640
- Şengör, A. M. C., Natal'in, B. A., Burtman, V. S., 1993. Evolution of the Altaid Tectonic Collage and Palaeozoic Crustal Growth in Eurasia. *Nature*, 364(6435): 299–307. <https://doi.org/10.1038/364299a0>
- Shao, J. A., He, G. Q., Tang, K. D., 2015. The Evolution of Permian Continental Crust in Northern Part of North China. *Acta Petrologica Sinica*, 31(1): 47–55 (in Chinese with English Abstract)
- Shao, J. A., Tang, K. D., He, G. Q., 2014. Early Permian Tectono-Palaeogeographic Reconstruction of Inner Mongolia, China. *Acta Petrologica Sinica*, 30(7): 1858–1866 (in Chinese with English Abstract)
- Söderlund, U., Patchett, P. J., Vervoort, J. D., et al., 2004. The ^{176}Lu Decay Constant Determined by Lu-Hf and U-Pb Isotope Systematics of Precambrian Mafic Intrusions. *Earth and Planetary Science Letters*, 219(3/4): 311–324. [https://doi.org/10.1016/s0012-821x\(04\)00012-3](https://doi.org/10.1016/s0012-821x(04)00012-3)
- Song, B., Zhang, Y. H., Wang, Y. S., et al., 2002. Mount Making and Procedure of the SHRIMP Dating. *Geological Review*, 48(Suppl.): 26–30 (in Chinese with English Abstract)
- Sun, S. S., McDonough, W. F., 1989. Chemical and Isotopic Systematics of Oceanic Basalts: Implications for Mantle Composition and Processes. *Geological Society, London, Special Publications*, 42(1): 313–345. <https://doi.org/10.1144/gsl.sp.1989.042.01.19>
- Tang, K. D., 1990. Tectonic Development of Paleozoic Foldbelts at the North Margin of the Sino-Korean Craton. *Tectonics*, 9(2): 249–260. <https://doi.org/10.1029/tc009i002p00249>
- Tang, K. D., 1992. Tectonic Evolution and Metallogenic Regularity of the Fold Belt in the North of the North China Plate. Peking University Press, Beijing (in Chinese)
- Wang, Y. M., Han, B. F., Griffin, W. L., et al., 2012. Post-Entrainment Mineral-Magma Interaction in Mantle Xenoliths from Inner Mongolia, Western North China Craton. *Journal of Earth Science*, 23(1): 54–76. <https://doi.org/10.1007/s12583-012-0233-x>
- Whalen, J. B., Currie, K. L., Chappell, B. W., 1987. A-Type Granites: Geochemical Characteristics, Discrimination and Petrogenesis. *Contributions to Mineralogy and Petrology*, 95(4): 407–419. <https://doi.org/10.1007/bf00402202>
- Wiedenbeck, M., Allé, P., Corfu, F., et al., 1995. Three Natural Zircon Standards for U-Th-Pb, Lu-Hf, Trace Element and REE Analyses. *Geostandards and Geoanalytical Research*, 19(1): 1–23. <https://doi.org/10.1111/j.1751-908x.1995.tb00147.x>
- Wu, F. Y., Li, X. H., Yang, J. H., et al., 2007. Discussions on the Petrogenesis of Granites. *Acta Petrologica Sinica*, 23(6): 1217–1238 (in Chinese with English Abstract)
- Wu, Y. B., Zheng, Y. F., 2004. Genetic of Zircon and Its Constraints on Interpretation of U-Pb Age. *Chinese Science Bulletin*, 49(16): 1589–1604 (in Chinese)
- Xiao, W. J., Windley, B. F., Hao, J., et al., 2003. Accretion Leading to Collision and the Permian Solonker Suture, Inner Mongolia, China: Termination of the Central Asian Orogenic Belt. *Tectonics*, 22(6): 1069. <https://doi.org/10.1029/2002tc001484>
- Xiao, W. J., Windley, B. F., Huang, B. C., et al., 2009. End-Permian to Mid-Triassic Termination of the Accretionary Processes of the Southern Altai: Implications for the Geodynamic Evolution, Phanerozoic Continental Growth, and Metallogeny of Central Asia. *International Journal of Earth Sciences*, 98(6): 1189–1217. <https://doi.org/10.1007/s00531-008-0407-z>
- Xu, B., Charvet, J., Chen, Y., et al., 2013. Middle Paleozoic Convergent Orogenic Belts in Western Inner Mongolia (China): Framework, Kinematics, Geochronology and Implications for Tectonic Evolution of the Central Asian Orogenic Belt. *Gondwana Research*, 23(4): 1342–1364. <https://doi.org/10.13039/501100001809>
- Xu, B., Chen, B., 1997. Framework and Evolution of the Middle Paleozoic Orogenic Belt between Siberian and North China Plates in Northern Inner Mongolia. *Science in China Series D: Earth Sciences*, 40(5): 463–469. <https://doi.org/10.1007/bf02877610>
- Xu, B., Zhao, P., Bao, Q. Z., et al., 2014. Preliminary Study on the Pre-Mesozoic Tectonic Unit Division of the Xing-Meng Orogenic Belt (XMOB). *Acta Petrologica Sinica*, 30(7): 1841–1857 (in Chinese with English Abstract)
- Zhang, X. H., Zhai, M. G., 2010. Magmatism and Its Metallogenic Effects during the Paleozoic Continental Crustal Construction in Northern North China: An Overview. *Acta Petrologica Sinica*, 26(5): 1329–1341 (in Chinese with English Abstract)
- Zhang, X. H., Zhang, H. F., Tang, Y. J., et al., 2006. Early Triassic A-Type Felsic Volcanism in the Xilinhaote-Xiwuqi, Central Inner Mongolia: Age, Geochemistry and Tectonic Implications. *Acta Petrologica Sinica*, 22(11): 2769–2780 (in Chinese with English Abstract)
- Zhao, P., Chen, Y., Xu, B., et al., 2013. Did the Paleo-Asian Ocean between North China Block and Mongolia Block Exist during the Late Paleozoic? First Paleomagnetic Evidence from Central-Eastern Inner Mongolia, China. *Journal of Geophysical Research: Solid Earth*, 118(5): 1873–1894. <https://doi.org/10.13039/501100001809>
- Zhao, P., Xu, B., Tong, Q. L., et al., 2016. Sedimentological and Geochronological Constraints on the Carboniferous Evolution of Central Inner Mongolia, Southeastern Central Asian Orogenic Belt: Inland Sea Deposition in a Post-Orogenic Setting. *Gondwana Research*, 31: 253–270. <https://doi.org/10.13039/501100001809>
- Zhou, W. X., Li, S. C., Ge, M. C., et al., 2016. Geochemistry and Zircon Geochronology of a Gabbro-Granodiorite Complex in Tongxunlian, Inner Mongolia: Partial Melting of Enriched Lithosphere Mantle. *Geological Journal*, 51(1): 21–41. <https://doi.org/10.1002/gj.2603>